On the Incorporation of Friction Into a Simultaneously Coupled Time Domain Model of a Rigid Rotor Supported by Air Foil Bearings

Sebastian von Osmanski, Jon S. Larsen, Ilmar F. Santos

Despite decades of research, the dynamics of air foil bearings (AFBs) are not yet fully captured by any model, suggesting that the fundamental mechanisms of the AFB and their relative merits are not yet fully understood. The recent years have seen promising results from nonlinear time domain models, allowing the dynamic pressure–compliance interaction and the unsteady terms of the compressible Reynolds equation to be considered.

By including the simple elastic foundation model (SEFM) in a fully coupled simultaneous time integration, the dynamics of a rotor supported by industrial AFBs have previously been modelled by the authors, leading to good agreement with experimental results. In this paper, the authors investigate the substitution of the SEFM for a new foil structure model which is based on directly measurable quantities and includes frictional energy dissipation in the foil structure. An important finding is that the incorporation of a friction model into the global model cannot be reconciled with a simultaneous time solution without the inclusion of the foil inertia. The resulting AFB model allows the effects of friction on AFB performance to be directly examined and leads to the questioning of friction's role and its significance to the operation of AFBs.

Nomenclature

AFB	Air Foil Bearing	$h, \tilde{h}$	Film height, $\tilde{h} = h/C$
CG	Center of Gravity	h_b	Bump foil height
DAE	Differential/Algebraic Equation	$h_c, \tilde{h}_c$	Film height (compliant), $\tilde{h}_c = h_c/C$
DOF	Degree of Freedom	$h_r, \tilde{h}_r$	Film height (rigid), $\tilde{h}_r = h_r/C$
FE	Finite Element	$h_s, \tilde{h}_s$	Slope height, $\tilde{h}_s = h_s/C$
ODE	Ordinary Differential Equation	k	Stiffness
SEFM	Simple Elastic Foundation Model	k_j, d_j	Truss stiffness and damping,
$(\ddot{})$	Time derivative, $d^2/d\tau^2$		$j \in \{1, 1b, 2, 3, 3b, 4\}$
$(\dot{})$	Time derivative, $d/d\tau$	l_0	Bump half length
$\nabla\cdot$	Divergence	l_1, l_2	Distance from CG to bearings
∇	Gradient, $\nabla = \{\partial/\partial\theta, \ \partial/\partial\tilde{z}\}$	l_3, l_4	Distance from CG to discs
A, B	Bearings	m	Mass
C	Radial clearance	$p, \tilde{p}$	Film pressure, $\tilde{p} = p/p_a$
E_b	Young's modulus of bump foil material	p_a	Ambient pressure
E_t	Young's modulus of top foil material	t	Physical time
I	Mass moment of inertia	t_b	Thickness of bump foil
$L, \tilde{L}$	Bearing length, $\tilde{L} = L/R$	t_t	Thickness of top foil
N_p	Number of bearing pads	v_r	Relative sliding velocity
R	Journal radius	$x, y, z, \tilde{z}$	Cartesian coordinates, $\tilde{z} = z/R$
R_b	Bump radius of curvature	x_j	Generalised degree of freedom
S	Compressibility number, $S = 6\mu\omega/p_a \left(R/C\right)^2$	x_j	Relative displacement
S_b	Bump foil pitch	α	Bearing position, $\alpha = A, B$
$W, \tilde{W}$	Static load components, $\tilde{W} = 1/(p_a R^2)W$	γ	Friction function smoothing parameter
$\tilde{p}_m$	Nondimensional mean axial pressure	μ	Dynamic viscosity
e, ε	Journal eccentricity components, $\varepsilon = e/C$	μ_f	Coefficient of friction
f_N	Normal force function	ν_b	Poisson's ratio of bump foil material
f_μ	Friction force	ν_t	Poisson's ratio of top foil material
f_{μ_f}	Friction coefficient smoothing function	ω	Angular speed of journal

ψ	Film state variable (nondimensional), $\psi = \tilde{p}\tilde{h}$	$\boldsymbol{\Psi}$	Film state vector
ρ_b	Density of bump foil material	$\tilde{\mathbf{p}}$	Pressure vector
ρ_t	Density of top foil material	$\boldsymbol{\varepsilon}$	Eccentricity vector, $\{\varepsilon_{Ax}, \varepsilon_{Ay}, \varepsilon_{Bx}, \varepsilon_{By}\}^T$
τ	Dimensionless time, $\tau = \omega t$	$\mathbf{f}_\mu$	Vector of friction forces
θ	Circumferential angle	$\mathbf{f}_p$	Vector of pressure forces
θ'	Curvelinear coordinate, $\theta' = \theta R$	$\mathbf{g}()$	Nonlinear vector function
θ_0	Bump half angle	$\mathbf{r}$	Residual vector
θ_j	Truss transmission angle, θ_d or θ_{db}	$\mathbf{x}$	Foil displacement vector
θ_l	First pad leading edge angle	$\mathbf{y}$	Global state vector
θ_s	Inlet slope extend	$\mathbf{z}_1, \mathbf{z}_2$	Rotor state vectors, $\mathbf{z}_1 = \boldsymbol{\varepsilon}$, $\mathbf{z}_2 = \dot{\mathbf{z}}_1$
θ_t	First pad trailing edge angle	$\mathbf{0}$	Zero matrix
$\tilde{\theta}$	Dimensionless circumferential coordinate, $\tilde{\theta} = \theta'/R = \theta$	$\mathbf{A}_f, \tilde{\mathbf{A}}_f$	Foil structure system matrix
		$\mathbf{D}_f, \tilde{\mathbf{D}}_f$	Foil structure damping matrix
ζ	Damping ratio	$\mathbf{G}_r, \tilde{\mathbf{G}}_r$	Rotor gyroscopic matrix,
$\tilde{\mathbf{u}}$	Foil structure state space vector, $\tilde{\mathbf{u}} = \{\tilde{\mathbf{x}}^T \ \dot{\tilde{\mathbf{x}}}^T\}^T$		$\tilde{\mathbf{G}}_r = \omega^2 C/(p_a R^2)\mathbf{G}_r$
		$\mathbf{I}$	Identity matrix
$\mathbf{f}, \tilde{\mathbf{f}}$	Bearing force vector, $\mathbf{f} = \{\mathbf{f}_A^T, \ \mathbf{f}_B^T\}^T, \tilde{\mathbf{f}} = 1/(p_a R^2)\mathbf{f}$	$\mathbf{K}_f, \tilde{\mathbf{K}}_f$	Foil structure stiffness matrix
		$\mathbf{M}_f, \tilde{\mathbf{M}}_f$	Foil structure mass matrix
$\mathbf{f}_{ub}, \tilde{\mathbf{f}}_{ub}$	Unbalance force, $\tilde{\mathbf{f}}_{ub} = 1/(p_a R^2)\mathbf{f}_{ub}$	$\mathbf{M}_r, \tilde{\mathbf{M}}_r$	Rotor mass matrix, $\tilde{\mathbf{M}}_r = \omega^2 C/(p_a R^2)\mathbf{M}_r$
$\mathbf{s}$	Advection vector, $\mathbf{s} = \{S, \ 0\}^T$	$\boldsymbol{\Gamma}$	Fluidity matrix
$\mathbf{w}, \tilde{\mathbf{w}}$	Load vector, $\tilde{\mathbf{w}} = 1/(p_a R^2)\mathbf{w}$	$(\tilde{\ })$	Nondimensional quantity

1 Introduction

Practical application of gas lubrication appeared in the mid-1950s driven by its attractiveness to several emerging technologies and facilitated by improved experimental equipment together with the development of computerised numerical methods (Powell, 1970). The first gas bearings with compliant inner surfaces appeared in the mid-1960s and the air foil bearing (AFB) was introduced industrially by Garrret AiResearch in 1969 (Agrawal, 1997). The AFB offers several advantages compared to conventional rigid gas bearings, and it is a key component in NASA's efforts towards creating a completely oil-free turbine engine (NASA, 2001). NASA is interested in the AFB technology's weight-saving potentials in rotorcrafts and its high-temperature capabilities, but AFBs also present an environmentally friendly alternative in many applications of oil-lubricated high-speed rotating machinery.

The compliant nature of AFBs does, however, complicate the modelling of its dynamic characteristics and is capable of introducing undesirable nonlinear features. As the performance of AFB supported rotor–bearing systems is often limited by nonlinear phenomena, such as sub-synchronous vibrations driven by unbalance, reliable means for predicting the response are an essential prerequisite for further spread of the technology.

The majority of the literature on AFB modelling rests on the original contributions by Heshmat et al. (1983b,a), who introduced the simple elastic foundation model (SEFM). The original SEFM, as well as the refined version by Peng and Carpino (1993), was applied in a perturbation method framework introduced by Lund (1968) and hence relied on a linearisation of the reaction forces to effectively replace the bearing and fluid film with a spring–dashpot system. Such analyses are inherently restricted to an assumed small-amplitude periodic motion (Bonello and Pham, 2009), and recent work (Larsen et al., 2016) additionally suggests an inadequacy in the applied Taylor series expansion of the pressure field. Another commonality shared throughout much of the literature is equivalent viscous models for the energy dissipation in the compliant structure. This approximation is pivotal since sliding friction in the foil structure is widely assumed to constitute a major source of damping (Agrawal, 1997; San Andrs and Kim, 2007; Howard and San Andrs, 2011; Le Lez et al., 2009) and hence to be essential in the workings of the AFB.

Nonlinear time domain integration circumvents the limitations of the perturbation techniques and provides a basis for the incorporation of foil structure models without the assumption of viscous dissipation. Applying different foil structure models, but based on a decoupling of the fluid, rotor and foil structure equations, time domain models have been presented by for example Lee et al. (2009); Le Lez et al. (2009); Hoffmann et al. (2015). This approach introduces a demand for very small time steps and temporal convergence studies, which has been overcome using simultaneous formulations (Bonello and Pham, 2014b,a; Larsen and Santos, 2015; Larsen et al., 2015b). Several promising results have been presented from these simultaneous models, but they are, however, still relying on the SEFM and hence on the assumption of viscous dissipation.

Figure 1: Schematics and nomenclature of a rigid rotor supported by AFBs: (a) shaft, bearings and rotor discs for unbalance masses; and (b) detailed view of the bearing geometry.

In recent work by the authors (von Osmanski et al., 2017), a fully coupled simultaneously formulated AFB model including friction has been presented. The current work provides additional discussions on the necessity of foil mass inclusion and an assessment of three effects related to friction: (*a*) displacement of the static equilibrium; (*b*) introduction of a dynamic foil stiffness; and (*c*) dissipation of energy through sliding friction.

2   The Rotor–Bearing System

The presented model and the derived considerations are based on a test rig previously presented and described by the authors (Larsen et al., 2015a,b; Larsen and Santos, 2015; Larsen et al., 2016; von Osmanski et al., 2017). The rig comprises a near-symmetrical hollow rotor supported by two identical second generation Siemens AFBs as sketched in Fig. 1a. The illustrated permanent magnets are part of the electrical drive capable of rotating the shaft to approximately $30\,\mathrm{kRPM}$ and the discs at each of the shaft's extremities allow unbalance mass to be added. As observed from the AFB geometry (Fig. 1b), the foil structure is segmented into three pads fixed to the bearing housing at their leading edges. The dimensions and mechanical properties as used throughout this paper are listed in Table 1.

3   Mathematical Model of the Rotor and the Fluid Film

As the dynamics of the support structure is not considered, modelling of the rotor–bearing system requires three domains to be assessed: the rotor, the fluid film and the compliant structure of the AFBs. This paper concerns mainly the latter of these, hence only a brief exposition of the applied rotor and fluid film models will be made.

The operational range of the rig is limited by the electrical drive to $30\,\mathrm{kRPM}$, while the lowest free–free natural frequency of the assembled shaft is found to be approximately $1050\,\mathrm{Hz}$, hence a rigid shaft model is deemed adequate. This gives a four degrees of freedom (DOFs) model which is considered a system of first order ordinary differential equations (ODEs) as

$$\begin{Bmatrix} \dot{\mathbf{z}}_1 \\ \dot{\mathbf{z}}_2 \end{Bmatrix} = \begin{bmatrix} \mathbf{0} & \mathbf{I} \\ \mathbf{0} & \tilde{\mathbf{M}}_r^{-1}\tilde{\mathbf{G}}_r \end{bmatrix} \begin{Bmatrix} \mathbf{z}_1 \\ \mathbf{z}_2 \end{Bmatrix} + \begin{Bmatrix} \mathbf{0} \\ \tilde{\mathbf{M}}_r^{-1}(\tilde{\mathbf{w}} - \tilde{\mathbf{f}} + \tilde{\mathbf{f}}_{ub}) \end{Bmatrix}, \tag{1}$$

where the state vectors hold the rotor displacements and velocities at the bearing positions as

$$\mathbf{z}_1 = \boldsymbol{\varepsilon} = \{\varepsilon_{Ax}, \ \varepsilon_{Ay}, \ \varepsilon_{Bx}, \ \varepsilon_{By}\}^T \quad \text{and} \quad \mathbf{z}_2 = \dot{\mathbf{z}}_1 = \dot{\boldsymbol{\varepsilon}}. \tag{2}$$

The system matrix contains the dimensionless mass and gyroscopic matrices of the rotor, $\tilde{\mathbf{M}}_r$ and $\tilde{\mathbf{G}}_r$, while $\tilde{\mathbf{w}}$, $\tilde{\mathbf{f}}$ and $\tilde{\mathbf{f}}_{ub}$ represent the static load, integrated fluid film reaction forces and unbalance forces, respectively.

The fluid film formed between the shaft and compliant inner surface of the AFBs is assumed to be governed by the

Table 1: Geometry, material properties and operating conditions of the Siemens AFB test rig.

Shaft assembly			
Bearing A to CG, l_1	201.1 mm	Mass, $m = m_x = m_y$	21.1166 kg
Bearing B to CG, l_2	197.9 mm	Polar moment of inertia, I_{zz}	30.079×10^{-3} kg m^2
Unbalance A to CG, l_3	287.2 mm	Transverse moment of inertia, $I_{xx} = I_{yy}$	525.166×10^{-3} kg m^2
Unbalance B to CG, l_4	304.0 mm		
Bearing configuration			
Bearing radius, R	33.50 mm	First pad leading edge, θ_l	30°
Bearing length, L	53.00 mm	First pad trailing edge, θ_t	145°
Radial clearance, C	40 µm	Slope extend, θ_s	30°
Number of pads, N_p	3	Slope height, h_s	50 µm
Fluid properties			
Viscosity, μ	1.95×10^{-5} Pa s	Ambient pressure, p_a	1×10^5 Pa
Bump foil properties			
Bump foil thickness, t_b	0.13 mm	Bump foil pitch, S_b	7.00 mm
Bump foil half length, l_0	3.43 mm	Bump foil height, h_b	1.15 mm
Young's modulus E_b	207 GPa	Poisson's ratio, ν_b	0.3
Radius of curvature, R_b	5.7 mm	Coefficient of friction, μ_f	0.05
Density, ρ_b	8280 kg/m^3	Bump half angle, θ_0	37°
Top foil properties			
Top foil thickness, t_t	0.254 mm	Poisson's ratio, ν_t	0.3
Young's modulus E_t	2.07×10^{11} Pa	Density, ρ_t	8280 kg/m^3

isothermal, compressible, transient Reynolds equation:

$$\nabla \cdot \left(\tilde{p}\tilde{h}^3 \nabla \tilde{p} \right) = \nabla \cdot \left(\tilde{p}\tilde{h} \right) \mathbf{s} + 2S \frac{d}{d\tau} \left(\tilde{p}\tilde{h} \right), \tag{3}$$

where $S = 6\mu\omega/p_a \left(R/C \right)^2$ is the compressibility number, $\mathbf{s} = \{S, \ 0\}^T$ is the advection vector and the film height $\tilde{h}$ is divided into a rigid and a compliant contribution as first suggested by Heshmat et al. (1983b):

$$\tilde{h} = \tilde{h}_r(\varepsilon_x, \varepsilon_y, \tilde{\theta}) + \tilde{h}_c. \tag{4}$$

The rigid contribution $\tilde{h}_r$ depends on the initial undeformed bearing geometry as illustrated in Fig. 1b and is given by e.g. von Osmanski et al. (2017), while the compliant contribution $\tilde{h}_c$ is treated in the following sections.

Following a partial substitution of ψ for $\tilde{p}\tilde{h}$ as introduced in Bonello and Pham (2014a,b), the fluid film partial differential equation Eq. (3) is spatially discretised using a finite element (FE) scheme. This gives a system of nonlinear ODEs in the film state variable time derivative vector $\dot{\boldsymbol{\psi}}_\alpha$ for each bearing $\alpha = A, B$

$$\boldsymbol{\Gamma}_\alpha \dot{\boldsymbol{\psi}}_\alpha = \mathbf{r}_\alpha \left(\dot{\boldsymbol{\psi}}_\alpha, \boldsymbol{\psi}_\alpha \right), \tag{5}$$

where the fluidity matrix $\boldsymbol{\Gamma}_\alpha$ is constant for a given angular velocity, while the residual vector $\mathbf{r}_\alpha$ depends on both the pressures, the film heights and the film heights' temporal derivatives.

4 Modelling of the Foil Structure

In the first time domain model presented by Larsen et al. (2015b); Larsen and Santos (2015) as well as in the presented models by Bonello and Pham (2014a,b), the compliant height contribution $\tilde{h}_c$ in Eq. (4) is supplied using the SEFM. This is numerically efficient, but implies that (*a*) the foil structure's energy dissipation is modelled as being viscous using an equivalent rotor-speed based loss factor; (*b*) the stiffness is linear and independent of both deformation and frequency; and (*c*) neighbouring points in the foil are assumed to deform independently. Other authors, such as Hoffmann et al. (2015); San Andrs and Kim (2009), have applied the SEFM merely to the underlying bump foil structure while incorporating more comprehensive models for the top foil. In this case, the top foil's bending stiffness couples the deflections of neighbouring points, but any bump–bump interaction effects are still neglected. An objective of the present work has hence been to discard the SEFM entirely in favour of a more general foil structure model. This model should facilitate the inclusion of friction, allow for a simultaneous solution of the equation system and be sufficiently efficient to permit time integration.

4.1 Friction Models

Sliding friction in the foil structure is widely assumed to be an important mechanism in AFBs (Agrawal, 1997; San Andrs and Kim, 2007; Howard and San Andrs, 2011; Le Lez et al., 2009); consequently, a friction model is included in the present work. Time integration of friction phenomena is difficult due to the nonlinear behaviour of the friction force near zero velocity and/or zero normal force. The potentially applicable friction models available in the literature can be roughly divided into three categories: stick-slip bookkeeping with alternating boundary conditions (Tariku and Rogers, 2001; Lee et al., 2009; Le Lez et al., 2007), nonlinear springs with moving reference points (Larsen et al., 2014) and continuous dynamic friction approximations (Oden and Martins, 1985; Makkar et al., 2005; Le Lez et al., 2008; Petrov and Ewins, 2003).

The stick-slip bookkeeping models introduce a differentiation between static and dynamic friction regimes in which either a boundary condition or a dynamic friction force is applied. These models hence rely on a continuous evaluation of the stick/slip states, and the abrupt changes inevitably caused by the change of state pose a challenge to numerical stability due to non-smooth, or even discontinuous, reaction and friction forces.

A friction model relying on nonlinear springs with moving reference points has also been suggested (Larsen et al., 2014) and shown to perform well in a quasi-static setting. The model handles the classical issue of determining the friction force at zero velocity, but has proven difficult to apply in a time domain framework due to the requirement of instantaneous detection of direction shifts.

The friction model applied in the current work belongs to the group of continuous dynamic friction approximations. These are based on expressions for the friction force f_μ of the form

$$f_\mu = f_N f_{\mu_f}(v_r), \tag{6}$$

where f_N is the normal force function and $f_{\mu_f}(v_r)$ is a smooth function of the sliding velocity v_r approximating the sign function. In the literature, various different functions can be found serving as sign approximations, including the inverse tangent, fractions similar to $v_r/(\gamma+|v_r|)$ and the hyperbolic tangent. The latter is used in the present as

$$f_{\mu_f}(v_r) = \mu_f \tanh(\gamma v_r), \tag{7}$$

where μ_f is a dynamic coefficient of friction and γ is a smoothing parameter controlling the slope near $v_r = 0$ and hence the level of approximation. As it can be seen, Eq. (7) provides no distinction between static and dynamic friction, but this could be achieved using the extended version given by Makkar et al. (2005).

Note that while the particular choice of friction model and smoothing function is debatable, an important point is that all of the assessed approaches share the common characteristic of velocity dependency. This is, to the best knowledge of the authors, the case for all existing and suitable friction models.

4.2 Structural Models

The compliant structure of the Siemens AFB consists of a bump foil and a top foil. For the present purpose, a simple one dimensional Bernoulli–Euler beam model is utilised for the top foil, as the main point of attention is the supporting bump foil structure. This approach leaves out any axial film height variations, but this has been shown to be a reasonable assumption (San Andrs and Kim, 2009).

For modelling of the bump foil, a straightforward plane FE approach requires several thousand DOFs per bump (Larsen et al., 2014), and is hence precluded from time integration purposes. A model reduction technique could possibly be applied, but here an efficient equivalent model by Le Lez et al. (2007) is used instead. In this model, the bump foil is represented using bar elements forming a simple truss with member stiffness coefficients k_1, k_2, k_3, k_4, k_{1b}, k_{3b} and force transmission angles θ_d, θ_{db}. These coefficients are calculated from 33 analytical expressions given by Le Lez et al. (2007) based on Castigliano's second theorem, and their values for the present geometry are given by von Osmanski et al. (2017).

In Table 2, the effective radial stiffness of the truss model for a nine-bump foil strip with dimensions from Table 1 is compared to results from a plane FE model based on a very accurate replication of the actual foil geometry. To emphasise the significance of the boundary condition at the foil–housing contacts, results are included for both rolling and pinned supports at this interface. The truss coefficients from Le Lez et al. (2007) are based

on the case of rolling supports, meaning that the bumps are allowed to slide circumferentially with no frictional resistance. Considering that the widely used expression by Walowit and Anno (1975) predicts a uniform stiffness of $0.88\,\mathrm{GN/m^3}$, the observed agreement between the truss and plane FE models is very good. If the foil–housing contacts are pinned, i.e. restrained from circumferential sliding, the effective truss stiffness is increased more than fivefold, while the plane FE model stiffness increases at least tenfold. A similar stiffening was observed by Feng and Kaneko (2010) and should be kept in mind as the two cases correspond to the extreme cases of zero friction and permanent sticking, respectively.

Table 2: Effective radial stiffness (for a uniform pressure) resulting from the truss model compared to a plane FE model for the two cases of (frictionless) rolling and pinned housing contact nodes.

Condition	Model	Effective normal stiffness for each bump [GN/m^3]								
		1	2	3	4	5	6	7	8	9
Sliding	Truss model	3.4	3.2	3.3	3.2	3.2	3.3	3.1	3.7	1.7
	Plane FE model	2.4	3.6	3.2	3.3	3.3	3.3	3.1	4.5	1.6
Pinned	Truss model	19.8	19.8	19.8	19.8	19.8	19.8	19.8	19.8	11.0
	Plane FE model	42.5	43.6	43.7	43.8	43.8	43.8	43.7	43.3	40.5

The truss model is formulated as a static model, meaning that it is governed by a system of algebraic equations. Coupling any (quasi-) static model directly to the differential equations governing the fluid film and the velocity dependent friction model gives rise to certain issues. These become evident if considering the simple mechanical system sketched in Fig. 2. It comprises a single point mass supported by four massless springs affected by a friction force in a configuration similar to the bump foil truss model. Writing out the governing equations in first order form, the following system can be obtained:

$$\begin{Bmatrix} 0 \\ 0 \\ 0 \\ \dot{x}_4 \\ \ddot{x}_4 \end{Bmatrix} = \begin{bmatrix} 2kc_\theta^2 & 0 & -kc_\theta^2 & 0 & 0 \\ 0 & k\left(3-2c_\theta^2\right) & kc_\theta s_\theta & -k & 0 \\ -kc_\theta^2 & kc_\theta s_\theta & kc_\theta^2+k & 0 & 0 \\ 0 & 0 & 0 & 0 & 1 \\ 0 & k/m & 0 & -k/m & 0 \end{bmatrix} \begin{Bmatrix} x_1 \\ x_2 \\ x_3 \\ x_4 \\ \dot{x}_4 \end{Bmatrix} - \begin{Bmatrix} 0 \\ 0 \\ f_N(x_1,x_2,x_3)f_{\mu_f}(\dot{x}_3) \\ 0 \\ 0 \end{Bmatrix} \quad \text{where} \quad \begin{aligned} c_\theta &= \cos\theta_d, \\ s_\theta &= \sin\theta_d. \end{aligned} \quad (8)$$

If friction is discarded, the upper three rows of Eq. (8) governing the massless truss are purely algebraic and hence provide neither velocities nor accelerations. Together with the two differential equations governing the point mass, this constitutes a system of semi-explicit differential/algebraic equations (DAEs). The DAEs represent a superset of the ODEs and are, in general, more troublesome since no guarantees on solution uniqueness or existence can be given as is the case for ODEs (see Poulsen et al. (2002); Petzold (1982)). Without friction, Eq. (8) is nevertheless very easy to solve. It could be condensed and solved as two first order ODEs, or it could be solved as is using a DAE solver.

Introducing friction, the solution of Eq. (8) becomes considerably more troublesome since the velocity required to determine the orientation and size of the friction force is not available. Obviously, this could be reconstructed using information from previous time steps using finite difference, but this would violate the requirement for a simultaneous formulation and reintroduce the demand for temporal convergence studies. In the case of a strictly positive normal force, the system could be considered as an implicit ODE (or DAE), but for any reasonable approximation to the sign function, this system is too stiff for practical purposes. In the actual AFB model, the case of zero normal force, implying zero friction force for any sliding velocity, would furthermore have to be spanned leaving the very structure of the equation system state dependent.

From a physical point of view, the fundamental issue is the lack of inertia to smooth out the displacements caused by the rapidly changing friction forces in the vicinity of zero sliding velocity. As a remedy, it is therefore natural to introduce the foil mass, even though this is per se insignificant to the overall rotordynamic response. Lumping the bump foil mass onto the truss structure (giving a diagonal mass matrix) the equations are remoulded from algebraic to differential with sliding velocities directly available. Coupling the obtained bump foil differential equations to the (also dynamic) Bernoulli–Euler beam top foil model and the friction model, the overall foil structure is assembled as visualised in Fig. 3. Notice that viscous dampers have also been introduced in the truss. These are principally undesired as a main objective is to model frictional instead of viscous dissipation, but a slight structural damping has proven numerically necessary due to the very high natural frequencies in the foil ranging up to around $500\,\mathrm{kHz}$. The frequency range of interest for the rotordynamic response goes to around $500\,\mathrm{Hz}$, and is hence well separated from the first natural frequency of the foil structure at around $2\,\mathrm{kHz}$. This allows a proportional damping,
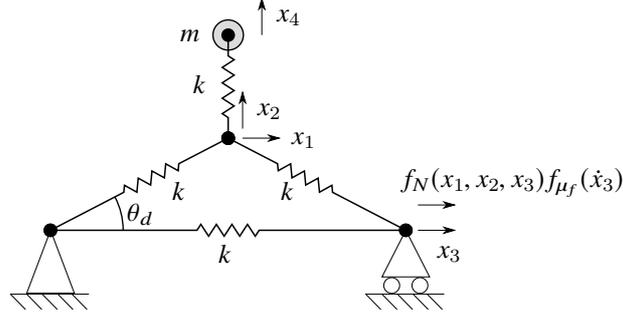
Figure 2: Mechanical system illustrating the challenges of using a massless foil model. It comprises a point mass (governed by a second order differential equation) supported by a massless truss (governed by four algebraic equations) subject to a friction force.
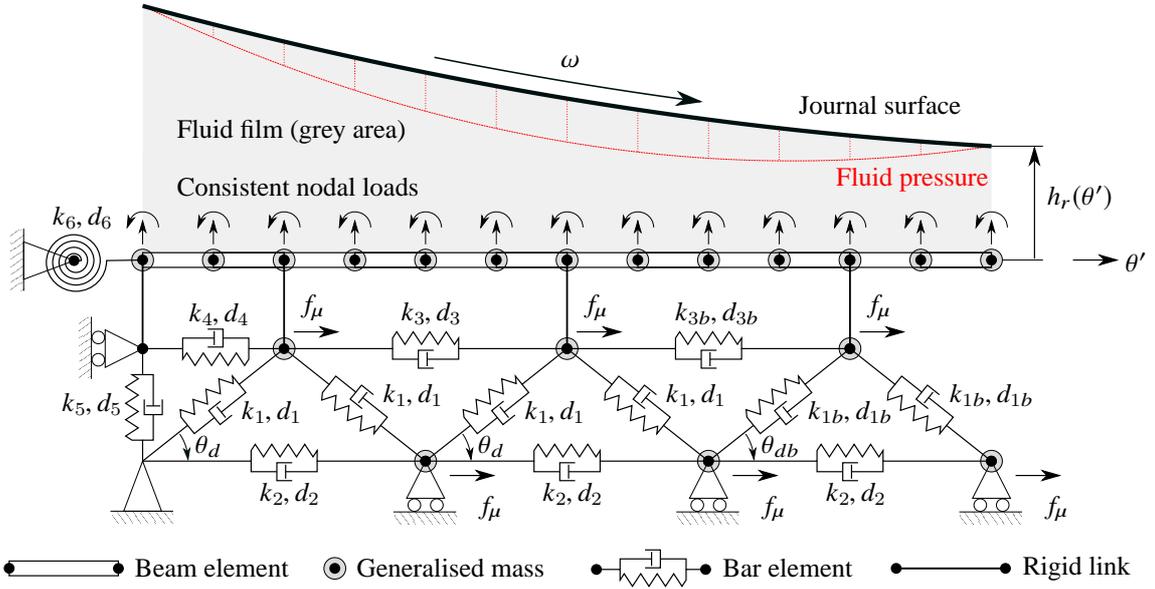

Figure 3: Illustration of the foil structure model for three bumps interacting with the journal through the generated fluid film (grey area). k_j, d_j denote the truss element stiffness and damping, while θ_j are the transmission angles and f_μ represents the friction forces. Notice that the last bump uses different coefficients than the remaining ones.

providing a damping ratio of $\zeta = 0.001$ at $500\,\mathrm{Hz}$, to be introduced to effectively dampen out the foil structure dynamics while leaving the dynamics of interest virtually unaffected.

Collecting the DOFs of the foil structure for each bearing $\alpha = A, B$ into the foil state vector $\tilde{\mathbf{u}}_\alpha$, the system of first order nonlinear ODEs governing the structure in Fig. 3 can be written as

$$
\dot{\tilde{\mathbf{u}}}_\alpha = \overbrace{\begin{bmatrix} \mathbf{0} & \mathbf{I} \\ -\tilde{\mathbf{M}}_f^{-1}\tilde{\mathbf{K}}_f & -\tilde{\mathbf{M}}_f^{-1}\tilde{\mathbf{D}}_f \end{bmatrix}}^{\tilde{\mathbf{A}}_f} \tilde{\mathbf{u}}_\alpha + \left\{ \begin{array}{c} \mathbf{0} \\ \tilde{\mathbf{M}}_f^{-1}\left(\mathbf{f}_\mu\left(\tilde{\mathbf{u}}_\alpha, \dot{\tilde{\mathbf{u}}}_\alpha, \tilde{\mathbf{p}}_\alpha\right) + \mathbf{f}_p\left(\tilde{\mathbf{p}}_\alpha\right)\right) \end{array} \right\},
\tag{9}
$$

where $\tilde{\mathbf{M}}_f$, $\tilde{\mathbf{D}}_f$ and $\tilde{\mathbf{K}}_f$ are the mass, (proportional-) damping and stiffness matrices of the foil structure, respectively. The vector function $\mathbf{f}_\mu$ represents the friction forces at the contact nodes given from Eq. (6) and the vector function $\mathbf{f}_p$ represents the work equivalent nodal loads on the top foil stemming from the fluid film pressure $\tilde{\mathbf{p}}_\alpha$.
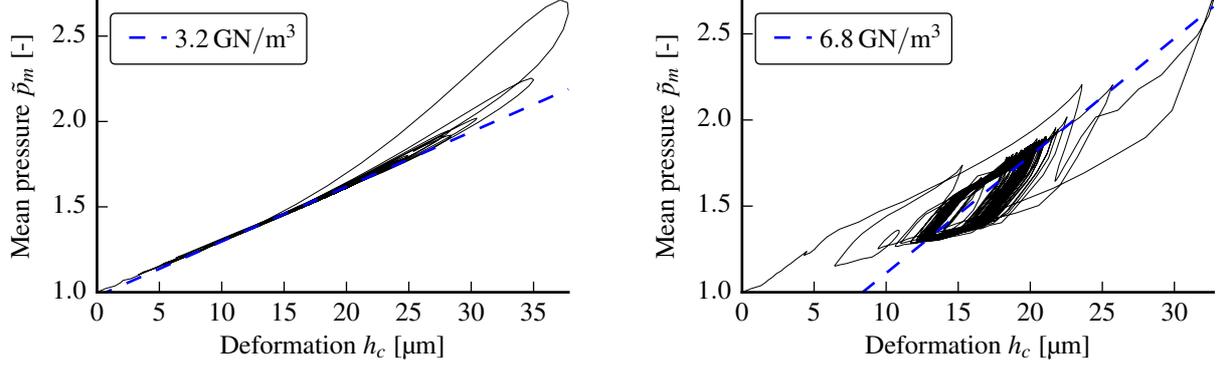
Figure 4: Hysteresis curves at the summit of bump three in the second pad segment ($\theta = 180°$) for $0.5\,\mathrm{s}$ of simulation from a rotor drop from the centre with (left) and without (right) friction. The dashed lines are fits to the last $0.125\,\mathrm{s}$ and indicate the local effective foil stiffness.

5   Structure of the Assembled Equation System

The three sets of first order ODEs representing the rotor, fluid and foil structure domains given from Eq. (1), Eq. (5) and Eq. (9) are now coupled. For this purpose, the global state vector

$$\mathbf{y} = \left\{ \boldsymbol{\psi}_A^T \quad \boldsymbol{\psi}_B^T \quad \tilde{\mathbf{u}}_A^T \quad \tilde{\mathbf{u}}_B^T \quad \mathbf{z}_1^T \quad \mathbf{z}_2^T \right\}^T, \tag{10}$$

is introduced, using which a single system of nonlinear first order ODEs can be written as

$$\begin{Bmatrix} \dot{\boldsymbol{\psi}}_A \\ \dot{\boldsymbol{\psi}}_B \\ \dot{\tilde{\mathbf{u}}}_A \\ \dot{\tilde{\mathbf{u}}}_B \\ \dot{\mathbf{z}}_1 \\ \dot{\mathbf{z}}_2 \end{Bmatrix} = \begin{bmatrix} \mathbf{0} & \cdots & \cdots & \cdots & \cdots & \mathbf{0} \\ \vdots & \cdots & \cdots & \cdots & \cdots & \vdots \\ \vdots & \vdots & \tilde{\mathbf{A}}_f & \mathbf{0} & \cdots & \vdots \\ \vdots & \vdots & \mathbf{0} & \tilde{\mathbf{A}}_f & \vdots & \mathbf{0} \\ \vdots & \vdots & \cdots & \cdots & \mathbf{0} & \mathbf{I} \\ \mathbf{0} & \cdots & \cdots & \mathbf{0} & \tilde{\mathbf{M}}_r^{-1}\tilde{\mathbf{G}}_r & \mathbf{0} \end{bmatrix} \begin{Bmatrix} \boldsymbol{\psi}_A \\ \boldsymbol{\psi}_B \\ \tilde{\mathbf{u}}_A \\ \tilde{\mathbf{u}}_B \\ \mathbf{z}_1 \\ \mathbf{z}_2 \end{Bmatrix} + \begin{Bmatrix} \mathbf{g}_{\dot{\psi}A}(\boldsymbol{\psi}_A, \mathbf{z}_1, \mathbf{z}_2, \tilde{\mathbf{u}}_A) \\ \mathbf{g}_{\dot{\psi}B}(\boldsymbol{\psi}_B, \mathbf{z}_1, \mathbf{z}_2, \tilde{\mathbf{u}}_B) \\ \mathbf{g}_{\dot{u}A}(\boldsymbol{\psi}_A, \mathbf{z}_1, \tilde{\mathbf{u}}_A, \dot{\tilde{\mathbf{u}}}_A) \\ \mathbf{g}_{\dot{u}B}(\boldsymbol{\psi}_B, \mathbf{z}_1, \tilde{\mathbf{u}}_B, \dot{\tilde{\mathbf{u}}}_B) \\ \mathbf{0} \\ \tilde{\mathbf{M}}_r^{-1}(\tilde{\mathbf{w}} - \tilde{\mathbf{f}} + \tilde{\mathbf{f}}_{ub}) \end{Bmatrix} . \tag{11}$$

The nonlinear functions $\mathbf{g}_{\dot{\psi}\alpha}$ on the right hand side of the upper equations representing the fluid film are defined from Eq. (5), while those in the midmost rows representing the foil structure, $\mathbf{g}_{\dot{u}\alpha}$, are given as the nonlinear part of Eq. (9).

It should be noted that the numerical time integration of the coupled equation system given from Eq. (11) is a nontrivial task. To make the presented foil model extension practically feasible, considerable prior optimisation of the SEFM based time integration code has been necessary. Through these efforts, the SEFM based simulation times has been reduced from days to minutes; but with the new foil structure, especially the friction model, the relevant simulations nevertheless take in the order of 24 hours to complete.

6   Results & Discussion

To provide insight into the behaviour of the foil model and the influence of friction, a rotor drop from the bearing centres with a high level of unbalance at $20\,\mathrm{kRPM}$ is simulated for $0.5\,\mathrm{s}$ with and without friction. In Fig. 4, the mean axial pressure $\tilde{p}_m$ is plotted as a function of the top foil deformation h_c at $\theta = 180°$. This point is in the heaviest loaded region and coincident with the summit of bump three in the second pad. Setting γ to zero, effectively deactivating the friction model, the foil behaves linearly and no friction-induced hysteresis is present. Fitting a line to the last $125\,\mathrm{ms}$ reveals a local stiffness of $3.2\,\mathrm{GN/m^3}$, which is very close to the statically obtained values from Table 2. Activating the friction model using $\gamma = 10^4$, a hysteresis loop opens up and the fit now gives a line passing diagonally through the hysteresis loop indicating an increase in effective stiffness to $6.8\,\mathrm{GN/m^3}$.

In Fig. 5, the vertical eccentricity ratio in bearing A is plotted during the first and last $40\,\mathrm{ms}$ of the rotor drop simulation both with and without friction. In the transient part, the inclusion of friction lowers the displacement
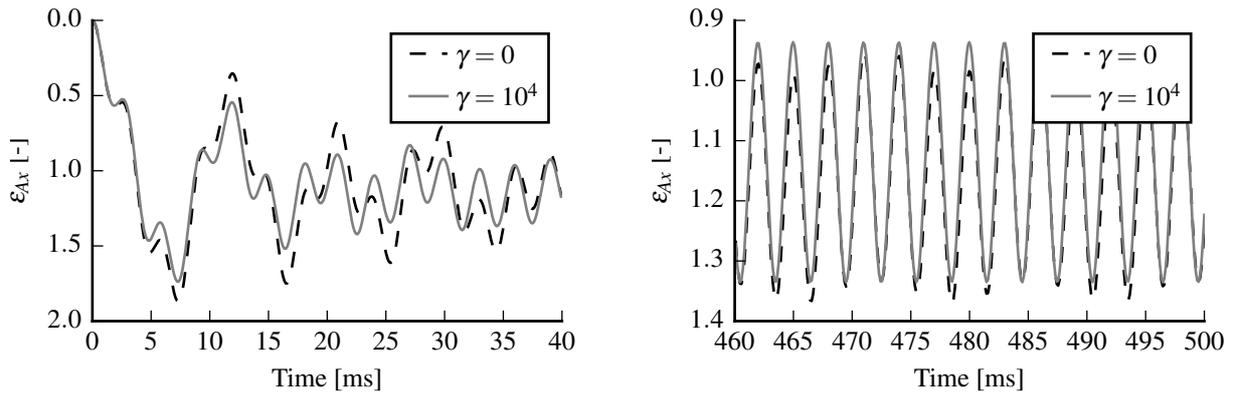
Figure 5: Vertical eccentricity ratio ε_{Ax} with friction ($\gamma = 10^4$) and without ($\gamma = 0$) friction. The first $40\,\mathrm{ms}$ after the rotor drop are shown to the left, while the final $40\,\mathrm{ms}$, where steady state has set in, are shown to the right.
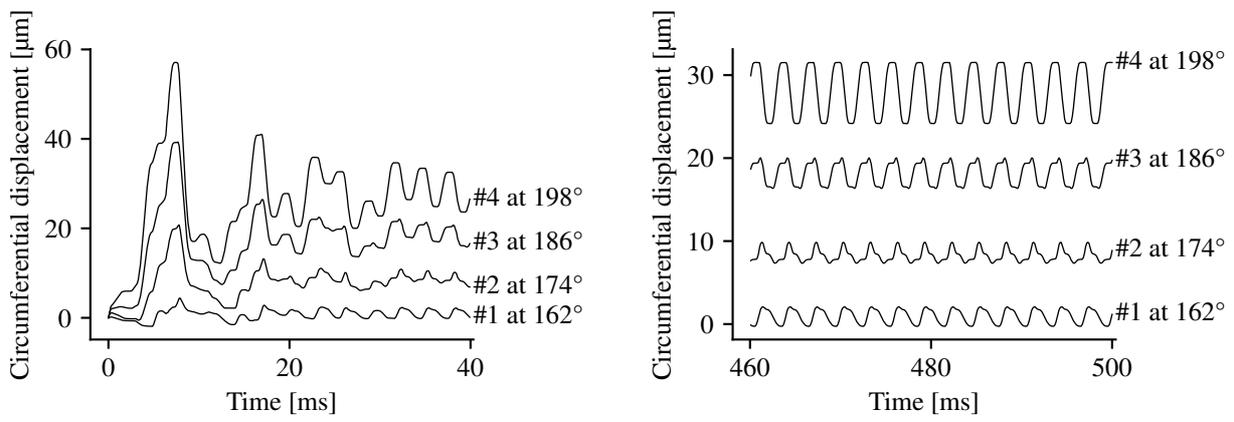

Figure 6: Circumferential displacement, i.e. sliding, of the bump foil–housing contact nodes of the four leading bumps in pad segment two. The left plot shows the first $40\,\mathrm{ms}$ after the rotor drop, while the right plot shows the final $40\,\mathrm{ms}$ of the simulation where steady state has been reached.

amplitudes, but almost identical steady states are eventually reached. This indicates that the equilibrium position is determined by the structural stiffness alone. This is in the order of 3–$4\,\mathrm{GN/m^3}$ and hence much lower than the equivalent SEFM stiffness of $9\,\mathrm{GN/m^3}$ used by Larsen and Santos (2015). The value of $9\,\mathrm{GN/m^3}$ was based on a number of "engineering assumptions" and was intended by Larsen and Santos (2015) to represent the dynamic foil stiffness, but as the applied model made no distinction between static and dynamic behaviour, this resulted in equilibrium points lying much higher than those obtained from the present model. If the effective static stiffness of the foil structure is in fact closer to $9\,\mathrm{GN/m^3}$, as suggested by the agreement to experimental results, the foil structure must, at least partly, be sticking.

Fig. 6 shows the circumferential sliding displacement for the first four bump foil–housing contact nodes in the second pad during the first and last $40\,\mathrm{ms}$. The presence of friction is evident in both plots from the characteristic flattened peaks and valleys related to the sign change of the friction forces. As both the mean displacements and the dynamic displacement amplitudes increase along the pad (this is also true for the remaining five bumps), the frictional energy dissipation will be largest for the bumps closest to the trailing edge.

The original motivation for introducing a friction model was twofold: *(a)* to circumvent the requirement for an empirically determined and constant equivalent stiffness; and *(b)* to avoid the inclusion of an empirical mechanical loss factor. It is evident from Fig. 4 that the friction model provides damping and that it increases the effective dynamic stiffness. It has, however, also been shown that the friction induced dynamic stiffness does not affect the equilibrium position. This means that the present AFB model results in steady state rotor eccentricities determined solely by the structural foil stiffness, while its dynamic characteristics at this equilibrium are influenced by friction. The effect is sketched in Fig. 7, where the left plot shows the radial deflection of a bump subjected to the load profile shown to the right. When loading up, point "A" is reached tracking the upper edge of the global hysteresis loop, where the effective stiffness is that of the sliding structure plus a frictional contribution. Ramping down the load, a line parallel to the right edge of the global loop is tracked to point "B" while the direction of sliding
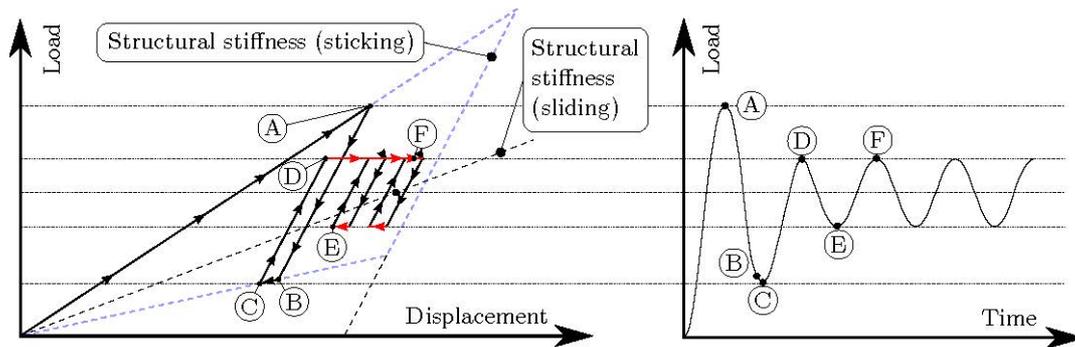
Figure 7: Sketch of the frictional drift present for the dynamic friction model. The right plot depicts a hypothetical load profile applied to a single bump and the left plot is the resulting displacement.

and hence the frictional force is reversed. Ideally, the effective stiffness is here close to that of a pinned bump, as no sliding should occur while the friction force changes direction. Note that the friction force crosses zero and changes direction as the dashed line indicating the sliding bump stiffness is crossed. Further decreasing the load from "B", the global hysteresis loop is tracked until "C" while the contact slides. Increasing the load to "D", the same stiffness as between "A" and "B" is experienced, but as the load is lowered from "D" towards "E", a frictional force sign change is required without any sliding. This is not possible for the dynamic friction model, meaning that the contact point will drift towards the frictionless equilibrium for each sign change made within the global loop. These drifts are marked in red in the plot (the short horizontal arrows) and even though their magnitude is dependent on the smoothing parameter, point "F" will eventually be reached. At this point, the oscillations take place around the same equilibrium as would have been reached without friction.

7   Conclusion

The paper has presented an alternative foil structure model for AFB simulation based on a truss representation of the bump foil originally proposed by Le Lez et al. (2007). The top foil is added using a simple one dimensional Bernoulli–Euler beam and a dynamic friction approximation is included to model frictional energy dissipation at the top foil–bump foil and bump foil–bearing housing interfaces. The usually applied foil structure models are static, i.e. represented by algebraic equations, but it is argued that the combination of a simultaneous solution in time and a friction model requires the inclusion of the foil inertia. This is achieved by augmenting the bump foil truss and top foil beam elements with lumped masses and subsequently to eliminate the entailed very high natural frequencies using stiffness proportional damping.

The new foil structure model is coupled to a nonlinear time domain model of a rigid shaft supported by two AFBs as a replacement for the SEFM. This allows the SEFM's inherent assumptions of viscous dissipation, constant stiffness and decoupled neighbouring points to be abandoned, and the empirically determined equivalent stiffness and loss coefficients of the SEFM can be replaced by directly measurable quantities.

The numerical results from the coupled model demonstrates that energy is dissipated by the friction model and that an increased effective dynamic stiffness is introduced. It is, however, evident that the dynamic stiffness caused by friction does not affect the obtained steady state position in the current model. This is reasonable considering the applied dynamic friction approximation, as this is not capable of representing true sticking and hence will allow net sliding until the equilibrium position dictated by the structural stiffness is reached. This is interesting, as the equivalent SEFM stiffness used by Larsen and Santos (2015) to obtain unbalance responses in very good agreement to experimental results, was based on the dynamic foil structure stiffness. In the SEFM, no distinction is made between the static structural stiffness and the friction induced dynamic stiffness, meaning that much higher foil compliances and rotor eccentricities are obtained using the new model than was the case using the SEFM (Larsen and Santos, 2015).

The agreement to experimental results achieved using the SEFM, with a constant equivalent stiffness much higher than that of a sliding bump foil structure, suggests that sticking is in fact a prevalent state. This would imply that the orbits predicted using the new foil structure model are too low-lying and, most importantly, that frictional dissipation is not as significant as generally assumed.

References

Agrawal, G. L.: Foil air/gas bearing technology - an overview. In: *ASME 1997 International Gas Turbine and Aeroengine Congress and Exhibition*, page 347, ASME (1997).

Bonello, P.; Pham, H. M.: A receptance harmonic balance technique for the computation of the vibration of a whole aero-engine model with nonlinear bearings. *Journal of Sound and Vibration*, 324, 1-2, (2009), 221–242.

Bonello, P.; Pham, H. M.: The efficient computation of the nonlinear dynamic response of a foilair bearing rotor system. *Journal of Sound and Vibration*, 333, 15, (2014a), 3459–3478.

Bonello, P.; Pham, H. M.: Nonlinear dynamic analysis of high speed oil-free turbomachinery with focus on stability and self-excited vibration. *Transactions of the ASME, Journal of Tribology*, 136, 4, (2014b), 041705.

Feng, K.; Kaneko, S.: Analytical model of bump-type foil bearings using a link-spring structure and a finite-element shell model. *Journal of Tribology*, 132, 2, (2010), 021706.

Heshmat, H.; Walowit, J. A.; Pinkus, O.: Analysis of gas lubricated compliant thrust bearings. *Journal of Lubrication Technology*, 105, 4, (1983a), 638.

Heshmat, H.; Walowit, J. A.; Pinkus, O.: Analysis of gas-lubricated foil journal bearings. *Journal of Lubrication Technology*, 105, 4, (1983b), 647–655.

Hoffmann, R.; Pronobis, T.; Liebich, R.: Non-linear stability analysis of a modified gas foil bearing structure. In: *Proceedings of the 9th IFToMM International Conference on Rotor Dynamics*, pages 1259–1276 (2015).

Howard, S. A.; San Andrs, L.: A new analysis tool assessment for rotordynamic modeling of gas foil bearings. *Journal of Engineering for Gas Turbines and Power*, 133, 2, (2011), 022505.

Larsen, J. S.; Hansen, A. J.; Santos, I. F.: Experimental and theoretical analysis of a rigid rotor supported by air foil bearings. *Mechanics & Industry*, 16, 1, (2015a), 106.

Larsen, J. S.; Nielsen, B. B.; Santos, I.: On the numerical simulation of nonlinear transient behavior of compliant air foil bearings. In: *Proceedings of the 11. International Conference on Schwingungen in Rotierenden Maschinen (SIRM2015)*, Magdeburg, Germany (23-25 February 2015b).

Larsen, J. S.; Santos, I. F.: On the nonlinear steady-state response of rigid rotors supported by air foil bearingstheory and experiments. *Journal of Sound and Vibration*, 346, (2015), 284–297.

Larsen, J. S.; Santos, I. F.; von Osmanski, S.: Stability of rigid rotors supported by air foil bearings: Comparison of two fundamental approaches. *Journal of Sound and Vibration*, 381, (2016), 179–191.

Larsen, J. S.; Varela, A. C.; Santos, I. F.: Numerical and experimental investigation of bump foil mechanical behaviour. *Tribology International*, 74, (2014), 46–56.

Le Lez, S.; Arghir, M.; Frene, J.: A new bump-type foil bearing structure analytical model. *Journal of Engineering for Gas Turbines and Power*, 129, 4, (2007), 1047–1057.

Le Lez, S.; Arghir, M.; Frene, J.: A dynamic model for dissipative structures used in bump-type foil bearings. *Tribology transactions*, 52, 1, (2008), 36–46.

Le Lez, S.; Arghir, M.; Frene, J.: Nonlinear numerical prediction of gas foil bearing stability and unbalanced response. *Journal of Engineering for Gas Turbines and Power*, 131, 1, (2009), 012503.

Lee, D.-H.; Kim, Y.-C.; Kim, K.-W.: The dynamic performance analysis of foil journal bearings considering coulomb friction: Rotating unbalance response. *Tribology Transactions*, 52, 2, (2009), 146–156.

Lund, J. W.: Calculation of stiffness and damping properties of gas bearings. *Journal of Lubrication Technology*, 90, 4, (1968), 793–803.

Makkar, C.; Dixon, W. E.; Sawyer, W. G.; Hu, G.: A new continuously differentiable friction model for control systems design. In: *Proceedings of the 2005 IEEE/ASME International Conference on Advanced Intelligent Mechatronics*, pages 600–605, IEEE, Monterey, California, USA (2005).

NASA: Creating a turbomachinery revolution: Research at Glenn enables an oil-free turbine engine, FS-2001-07-014-GRC (2001).

Oden, J. T.; Martins, J. A. C.: Models and computational methods for dynamic friction phenomena. *Computer Methods in Applied Mechanics and Engineering*, 52, 1, (1985), 527–634.

Peng, J. P.; Carpino, M.: Calculation of stiffness and damping coefficients for elastically supported gas foil bearings. *Journal of Tribology*, 115, 1, (1993), 20–27.

Petrov, E. P.; Ewins, D. J.: Generic friction models for time-domain vibration analysis of bladed discs. *American Society of Mechanical Engineers, International Gas Turbine Institute, Turbo Expo (Publication) IGTI*, 4, (2003), 223–233.

Petzold, L.: Differential/algebraic equations are not ODE's. *SIAM Journal on Scientific and Statistical Computing*, 3, 3, (1982), 367–384.

Poulsen, M. Z.; Thomsen, P. G.; Houbak, N.: *Structural analysis of DAEs*. Ph.D. thesis, Technical University of Denmark, Lyngby, Denmark (9 2002).

Powell, J. W.: A review of progress in gas lubrication. *Review of Physics in Technology*, 1, 2, (1970), 96–129.

San Andrs, L.; Kim, T. H.: Improvements to the analysis of gas foil bearings: Integration of top foil 1d and 2d structural models. In: *ASME Turbo Expo 2007: Power for Land, Sea, and Air*, vol. 5, pages 779–789, International Gas Turbine Institute, ASME, Montreal, Canada (2007).

San Andrs, L.; Kim, T. H.: Analysis of gas foil bearings integrating FE top foil models. *Tribology International*, 42, 1, (2009), 111–120.

Tariku, F. A.; Rogers, R. J.: Improved dynamic friction models for simulation of one-dimensional and two-dimensional stick-slip motion. *Journal of Tribology – Transactions of the ASME*, 123, 4, (2001), 661–669.

von Osmanski, S.; Larsen, J. S.; Santos, I. F.: A fully coupled air foil bearing model considering friction - theory & experiment. *Journal of Sound and Vibration*, 400, (2017), 660–679.

Walowit, J. A.; Anno, J. N.: *Modern developments in lubrication mechanics*. Applied Science Publishers London (1975).

Address: Department of Mechanical Engineering, Technical University of Denmark, 2800, Kgs. Lyngby, Denmark
E-mail addresses: `asvosm@mek.dtu.dk` (S. von Osmanski), `josla@mek.dtu.dk` (J.S. Larsen) and `ifs@mek.dtu.dk` (I.F. Santos)